

SCALABLE TRAINING FOR VECTOR-QUANTIZED NETWORKS WITH 100% CODEBOOK UTILIZATION

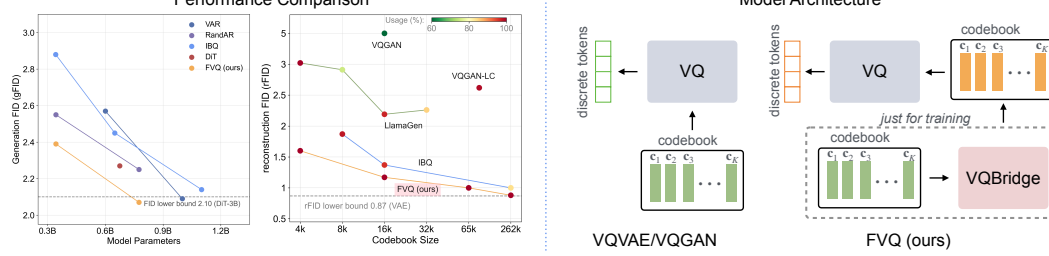
Yifan Chang^{1,4}Zheng Zhu³Jie Qin²Lin Ma²Limeng Qiao²Xingang Wang^{1,5}Xiaofeng Wang³¹CASIA²Meituan³GigaAI⁴UCAS⁵Luoyang Institute for Robot and Intelligent Equipment

Figure 1: **Performance comparison and model architecture.** **Left:** Performance comparison showing generation (FID) and reconstruction (rFID) quality across different methods. **Right:** Architectural comparison between baseline VQVAE/VQGAN and the proposed FVQ model, with VQBridge component for training.

ABSTRACT

Vector quantization (VQ) is a key component in discrete tokenizers for image generation, but its training is often unstable due to straight-through estimation bias, one-step-behind updates, and sparse codebook gradients, which lead to suboptimal reconstruction performance and low codebook usage. In this work, we analyze these fundamental challenges and provide a simple yet effective solution. To maintain high codebook usage in VQ networks (VQN) during learning annealing and codebook size expansion, we propose VQBridge, a robust, scalable, and efficient projector based on the map function method. VQBridge optimizes code vectors through a compress–process–recover pipeline, enabling stable and effective codebook training. By combining VQBridge with learning annealing, our VQN achieves full (100%) codebook usage across diverse codebook configurations, which we refer to as FVQ (FullVQ). Through extensive experiments, we demonstrate that FVQ is effective, scalable, and generalizable: it attains 100% codebook usage even with a 262k-codebook, achieves state-of-the-art reconstruction performance, consistently improves with larger codebooks, higher vector channels, or longer training, and remains effective across different VQ variants. Moreover, when integrated with LlamaGen, FVQ significantly enhances image generation performance, surpassing visual autoregressive models (VAR) by 0.5 and diffusion models (DiT) by 0.2 rFID, highlighting the importance of high-quality tokenizers for strong autoregressive image generation. <https://github.com/yfChang-cv/FVQ>

1 INTRODUCTION

The scalability of autoregressive models has been well demonstrated in large language models (Radford et al., 2018; Brown et al., 2020; Touvron et al., 2023; Grattafiori et al., 2024; Bai et al., 2023). Inspired by this, pioneering works (Esser et al., 2021; Yu et al., 2022; Ramesh et al., 2021; Tian et al., 2024) have explored the application of autoregressive models in visual generation tasks. To enhance scalability and reduce computational costs, a common approach (Van Den Oord et al., 2017; Razavi et al., 2019) involves introducing discrete tokenizers that employ vector quantization (VQ) to convert continuous images into discrete tokens. Autoregressive models are trained on these tokens in a self-supervised strategy to predict the next tokens. Generally, the reconstruction capability of the tokenizer directly determines the upper bound of the generative model’s performance (Esser

et al., 2021; Yu et al., 2024a). Therefore, the design of discrete tokenizers plays a crucial role in autoregressive visual generation.

However, due to the information loss introduced by vector quantization, the performance of discrete tokenizers has long been limited compared with continuous tokenizers (Kingma, 2013). The intuitive insight is that enlarging the codebook could reduce the information loss during quantization. Nevertheless, prior work (Yu et al., 2022; Sun et al., 2024; Ma et al., 2025) has shown that simply increasing the codebook size or code dimension often leads to codebook collapse, which causes a severe reduction in codebook usage and consequently undermines the generative capability of downstream models (Huh et al., 2023; Luo et al., 2024). Despite many efforts to mitigate this issue, when scaling to larger settings (e.g., codebook size of 262k and code dimension of 256) (Shi et al., 2025), full codebook usage remains unattainable and the performance is still unsatisfactory.

To address this issue, we revisit VQ from fundamental mechanism and three fundamental challenges (Huh et al., 2023), together with empirical observations that shed light on resolving them. VQ relies on the straight-through estimator (STE) (Bengio et al., 2013) to resolve the non-differentiability problem, but this introduces three additional challenges: straight-through estimation bias, one-step-behind update, and sparse codebook gradients. The first two challenges cause misalignment in optimization across the network, leading to instability, while sparse codebook gradients prevent the codebook from being sufficiently trained. In practice, only a small subset of code vectors are updated, which is the primary cause of collapse.

Surprisingly, based on our observations, these challenges can be effectively mitigated using only learning annealing and a sufficient powerful projector that jointly optimizes the codebook. Prior works (Zhu et al., 2024a;b) employ a linear layer as the projector for joint codebook optimization, showing some improvement. However, our further experiments reveal that a linear projector alone is fragile: it makes the network highly sensitive to the learning rate and insufficiently capable when scaling to larger codebooks. To enable robust and scalable VQ training, we propose a robust, scalable and efficient projector, called VQBridge, as shown in Figure 1. VQBridge adopts a compress–process–recover pipeline: it first compresses the set of code vectors into a smaller number, then models interactions via ViT blocks (Dosovitskiy et al., 2020), and finally recovers the vectors to the original codebook size and dimensionality. This design allows VQ to rapidly achieve and sustain 100% codebook usage for arbitrary codebook configurations, enabling effective optimization of VQ.

Using VQBridge combined with learning annealing, we conduct extensive experiments to validate its effectiveness, scalability, and generalization. On the ImageNet benchmark (Deng et al., 2009), FVQ consistently achieves 100% codebook usage across all configurations, including a 262k-codebook, while substantially enhancing the reconstruction performance of discrete tokenizers (rFID = 0.88), without introducing additional parameters or inference cost. FVQ exhibits strong scalability, with performance consistently improving as the codebook size, vector channel, and number of training epochs increase. Furthermore, the approach remains effective when applied to multi-code representation VQ (Lee et al., 2022; Tian et al., 2024), demonstrating robust generalization. Besides, FVQ leads to substantial improvements in generation performance: for instance, LlamaGen-XL improves FID from 3.39 to 2.07, outperforming comparable visual autoregressive models VAR (Tian et al., 2024) (FID=2.57) and diffusion models DiT (Peebles & Xie, 2023) (FID=2.27). These results highlight that even a vanilla autoregressive framework can achieve strong generation capabilities when the tokenizer exhibits high-quality reconstruction.

In summary, our contributions include:

1. We analyze the fundamental challenges arising from vector quantization and provide effective observations, leading to a simple yet scalable training framework (FVQ).
2. Through extensive experiments, we show that FVQ is effective, scalable, and generalizable. Specifically, it achieves 100% codebook usage across all configurations, attains state-of-the-art reconstruction performance, and consistently improves as the codebook size, vector channel, and number of training epochs increase, remains effective across different types of VQ.
3. We demonstrate that FVQ substantially enhances the generative capability of autoregressive models. Without any bells and whistles, a vanilla autoregressive framework equipped with FVQ outperforms advanced visual autoregressive models (VAR) and diffusion models (DiT).

2 BACKGROUND

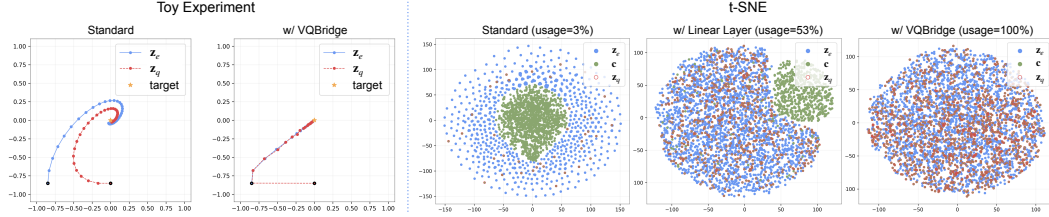


Figure 2: **Toy experiment and t-SNE visualization results.** **Left:** A dynamic vector quantization toy experiment where the target is a fixed optimization objective and the model is optimized with SGD. Using the standard method with only STE leads to a spiral trajectory, while VQBridge produces a piecewise linear trajectory. With VQBridge, \mathbf{z}_q closely follows \mathbf{z}_e , reducing their distance already in the early stages of training. **Right:** Due to sparse gradients from the codebook, the standard method achieves only 3% codebook usage. Adding a linear layer for joint optimization improves the usage but remains insufficient, whereas VQBridge achieves 100% usage.

Vector Quantized Network. A vector quantized network (VQN) contains Encoder $\mathcal{E}(\cdot)$, Vector Quantization Layer $\mathcal{Q}(\cdot, \cdot)$ and Decoder $\mathcal{D}(\cdot)$. Given a vector \mathbf{x} , the encoder maps it into a latent representation \mathbf{z}_e . The codebook is a collection of K code vectors, denoted as $\mathcal{C} = \{\mathbf{c}_1, \mathbf{c}_2, \dots, \mathbf{c}_K\}$, where each vector \mathbf{c}_i has same dimension as \mathbf{z}_e . In quantization layer $\mathcal{Q}(\cdot, \cdot)$, \mathbf{z}_e is quantized into \mathbf{z}_q by assigning it into a code vector from codebook \mathcal{C} using a distance measure $d(\cdot, \cdot)$:

$$\mathbf{z}_q = \mathbf{c}_x, \quad \text{where } x = \arg \min_i d(\mathbf{z}_e, \mathbf{c}_i). \quad (1)$$

Therefore, VQNs can be denoted:

$$\hat{\mathbf{y}} = \mathcal{D}(\mathcal{Q}(\mathcal{E}(\mathbf{x}), \mathcal{C})) = \mathcal{D}(\mathcal{Q}(\mathbf{z}_e, \mathcal{C})) = \mathcal{D}(\mathbf{z}_q). \quad (2)$$

VQNs predict the output $\hat{\mathbf{y}}$ and compute loss with target \mathbf{y} : $\mathcal{L}(\mathbf{y}, \hat{\mathbf{y}})$. The objective of VQNs is to optimize the following loss function:

$$\min_{\mathcal{E}, \mathcal{Q}, \mathcal{D}} \mathbb{E}_{(\mathbf{x}, \mathbf{y}) \sim \mathcal{T}} [\mathcal{L}_{task}(\mathcal{D}(\mathcal{Q}(\mathcal{E}(\mathbf{x}), \mathcal{C}))), \mathbf{y}], \quad (3)$$

where \mathcal{T} is training dataset. The extension to image reconstruction is straightforward by applying the formulation to 2D data; see Appendix F for details.

Optimization Challenge. Since the $\arg \min$ operation in the quantization layer $\mathcal{Q}(\cdot)$ is non-differentiable, a common approach is to apply the straight-through estimator (STE) during backpropagation (Bengio et al., 2013), which allows gradients to bypass the discrete operation:

$$\mathbf{z}_q = \mathbf{z}_e + sg[(\mathbf{z}_q - \mathbf{z}_e)], \quad (4)$$

where $sg[\cdot]$ is stop-gradient operation. In addition, a commitment loss (Van Den Oord et al., 2017) is introduced to ensure that the gradient flow on both sides of the quantization layer remains accurate:

$$\mathcal{L}_{cmt}(\mathbf{z}_e, \mathbf{z}_q) = d(\mathbf{z}_q, sg[\mathbf{z}_e]) + \beta d(\mathbf{z}_e, sg[\mathbf{z}_q]). \quad (5)$$

Although this approach makes the objective differentiable and thus optimizable, it introduces several additional challenges.

Challenge 1: Straight-Through Estimation Bias. The straight-through estimation error, defined as $\delta = \mathbf{z}_q - \mathbf{z}_e$, introduces bias into the training process. It directly affects the decoder $\mathcal{D}(\cdot)$ and indirectly impacts the encoder $\mathcal{E}(\cdot)$ through the commitment loss (Huh et al., 2023).

Challenge 2: One-step-behind Update. Through derivation (see Appendix D), we show that the commitment loss causes the model to align with historical representations instead of the current ones (Łańcucki et al., 2020; Huh et al., 2023). Specifically, the codebook is updated as

$$\mathbf{z}_q^{(t+1)} \leftarrow (1 - \eta) \cdot \mathbf{z}_q^{(t)} + \eta \cdot \mathbf{z}_e^{(t)}, \quad (6)$$

and the decoder is trained on the previous codebook output. This mismatch leads to a misalignment between the encoder and decoder. Ideally, both should be updated using the current representation:

$$\mathbf{z}_q^{(t+1)} \leftarrow (1 - \eta) \cdot \mathbf{z}_q^{(t)} + \eta \cdot \mathbf{z}_e^{(t+1)}. \quad (7)$$

Challenge 3: Sparse Codebook Gradients. The codebook \mathcal{C} suffers from sparse gradients—only the selected code vectors receive updates, while the unselected ones get no gradient signal and are likely to remain unused indefinitely (Zheng & Vedaldi, 2023; Shi et al., 2025). This results in codebook collapse and limited representational capacity.

We use a toy experiment to illustrate the impact of the STE. As shown in Figure 2, the optimization trajectories of \mathbf{z}_e and \mathbf{z}_q form a spiral shape, revealing hindered optimization (**Challenge 1 & 2**). Moreover, the t-SNE visualization further shows that directly applying the STE leads to low usage, with most codebook entries left unused. This phenomenon arises from the sparse gradients received by the codebook (**Challenge 3**).

3 METHODOLOGY

3.1 PRELIMINARY OBSERVATIONS

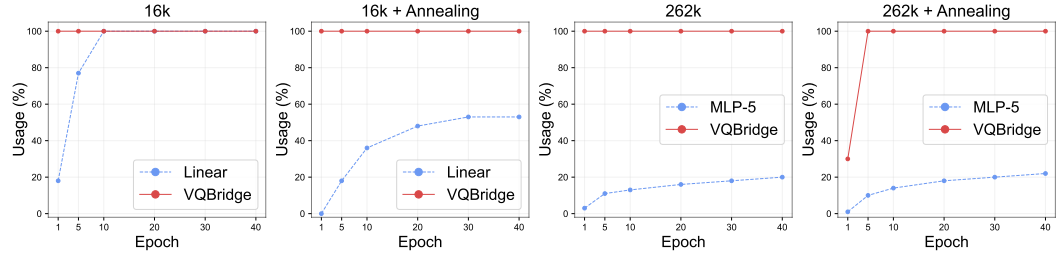


Figure 3: Codebook usage during training. With a codebook size of 16k, the linear-layer baseline can achieve 100% usage, but usage drops significantly when learning annealing is applied. With a larger codebook size of 262k, even a 5-layer MLP fails to maintain sufficient usage. In contrast, VQBridge rapidly achieves 100% usage under all configurations and with learning annealing, which greatly facilitates VQN optimization.

We denote the corresponding sets of \mathbf{z}_e , \mathbf{c} , and \mathbf{z}_q as \mathcal{P}_z , \mathcal{C}_z , and \mathcal{H}_z , respectively. The distance between the distributions of the two sets can be formally defined as

$$D(\mathcal{P}_z, \mathcal{C}_z) = \frac{1}{|\mathcal{P}_z|} \sum_{\mathbf{z}_i \in \mathcal{P}_z} \min_{\mathbf{c}_i \in \mathcal{C}_z} d(\mathbf{z}_i, \mathbf{c}_i).$$

Our work is based on the simple and effective linear reparameterization (Huh et al., 2023; Zhu et al., 2024a;b), which can be generalized as a mapping function $f(\cdot)$ from \mathcal{C}_z to a new set $\hat{\mathcal{C}}_z$, with joint optimization over \mathbf{c} : $\hat{\mathcal{C}}_z = f(\mathcal{C}_z)$. Consequently, the training objective shifts to minimizing the distance between \mathcal{P}_z and $\hat{\mathcal{C}}_z$: $D(\mathcal{P}_z, \hat{\mathcal{C}}_z)$. A smaller $D(\mathcal{P}_z, \hat{\mathcal{C}}_z)$ indicates a smaller estimation error δ . However, estimation error does not necessarily reflect optimization effectiveness, since a small number of active codebook vectors may lead to lower loss but fail to yield meaningful performance gains (Huh et al., 2023). Codebook usage can therefore serve as a complementary metric, as higher usage indicates that more vectors are effectively contributing, which is more informative.

Observation 1 *To mitigate the straight-through estimation bias, rapid alignment of the two distributions is crucial, reducing $D(\mathcal{P}_z, \mathcal{C}_z)$ early in training. Furthermore, estimation error must remain low for stable optimization. In practice, this requires using a larger codebook while maintaining high usage from early to late training. We present the effect of codebook size on the loss in Appendix C.*

Observation 2 *Learning annealing is necessary, as a smaller learning rate helps reduce the one-step-behind effect and improves the overall alignment of the model. We establish an upper bound on the effect of the one-step-behind update and demonstrate that learning annealing serves as an effective remedy. Further derivations are presented in Appendix E.*

Observation 3 *Linear layer is weak.* As shown in Figure 3, we observe that when a linear layer is used as the mapping function $f(\cdot)$, the codebook usage drops significantly during learning annealing. Additionally, under codebook scaling, the linear mapping struggles even more. Attempts to increase model capacity with a 5-layer MLP still result in poor usage. This suggests that the representational power of such mappings is inadequate for aligning the distributions of \mathcal{P}_z and $\hat{\mathcal{C}}_z$.

Based on the above observations, stable and scalable training of VQN requires a strong and robust mapping function $f(\cdot)$, combined with learning annealing. In the following section, we introduce our proposed design, referred to as VQBridge.

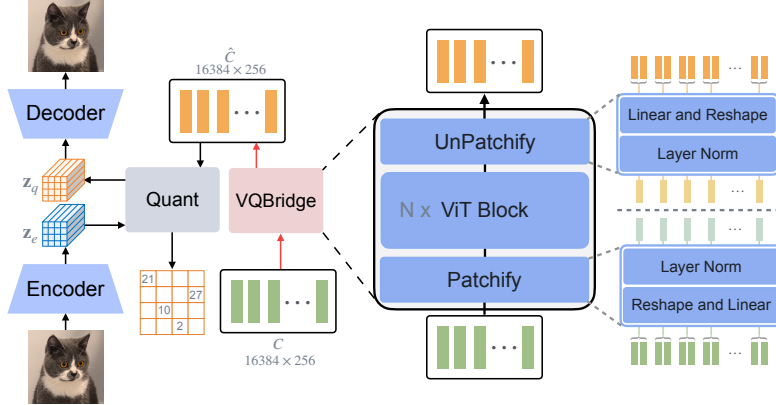


Figure 4: **FVQ framework overview.** VQBridge first applies 1D patchification to the code vectors, then performs global interaction using ViT blocks, and finally restores them to their original size.

3.2 VQBRIDGE DESIGN

The design objective of VQBridge is to achieve strong fitting capability, enabling rapid alignment between two distributions, while maintaining scalability and training stability. Inspired by the architecture of Diffusion Transformers (DiT) (Peebles & Xie, 2023), the module follows a compress–process–recover pipeline, where the compression step enables efficient scaling to large codebooks (*e.g.*, 262k entries). To simplify the problem, we assume that codebook \mathcal{C} and the mapped codebook $\hat{\mathcal{C}} = f(\mathcal{C})$ share the same size and vector channel. Details are provided in Figure 4.

First, we perform a 1D *patchify* operation. Given a codebook \mathcal{C} containing K code vectors, we divide it into p groups, each containing $\frac{K}{p}$ vectors. For each group, the vectors are compressed into a single vector via a shared linear projection $W_{\text{comp}} \in \mathbb{R}^{d \times d'}$, followed by a LayerNorm operation:

$$\mathbf{h}_g = \text{LN}(\mathbf{C}_g W_{\text{comp}}), \quad g = 1, \dots, p. \quad (8)$$

Next, N ViT blocks are applied as scalable layers to process the intermediate representation $\mathbf{H} \in \mathbb{R}^{p \times d'}$, enabling global information exchange and allowing the model to fit complex relationships between code vectors:

$$\mathbf{H}' = \text{ViT}^N(\mathbf{H}). \quad (9)$$

Finally, a 1D *unpatchify* operation restores the representation to its original size. Specifically, \mathbf{H}' is first normalized via LayerNorm, then expanded to p times its dimension through a shared linear projection $W_{\text{exp}} \in \mathbb{R}^{d' \times pd}$:

$$\tilde{\mathbf{H}} = \text{LN}(\mathbf{H}') W_{\text{exp}}, \quad (10)$$

followed by a reshape operation that converts each expanded vector back into p vectors within group:

$$\hat{\mathbf{C}} = \text{reshape}(\tilde{\mathbf{H}}) \in \mathbb{R}^{K \times d}. \quad (11)$$

This yields a codebook $\hat{\mathbf{C}}$ of the same size as the input to VQBridge, where the code vectors have undergone full mutual interaction.

Note that both VQBridge and the original codebook \mathcal{C} can be discarded after training, maintaining only the mapped codebook $\hat{\mathcal{C}}$. This implies that VQBridge introduces no additional computational overhead during inference, preserving the original VQN’s workflow and computational cost.

4 EXPERIMENTS

4.1 MAIN EXPERIMENTS

Table 1: **Reconstruction performance of different tokenizers on 256×256 ImageNet 50k validation set using the same Encoder and Decoder.** * trained on OpenImages (Kuznetsova et al., 2020). † trained for 330 epochs. ‡ trained for 120 epochs. We highlight the best results in bold and underline the second-best results.

Method	Tokens	Codebook Size	Vector Channel	rFID \downarrow	LPIPS \downarrow	Codebook Usage \uparrow
VQGAN (Esser et al., 2021)	16×16	1,024	256	7.94	—	44%
VQGAN (Esser et al., 2021)	16×16	16,384	256	4.98	0.17	5.9%
SD* (Rombach et al., 2022a)	16×16	16,384	8	5.15	—	—
MaskGIT (Chang et al., 2022)	16×16	1,024	256	2.28	—	—
LlamaGen (Sun et al., 2024)	16×16	16,384	8	2.19	0.14	97%
LlamaGen (Sun et al., 2024)	16×16	16,384	256	9.21	—	0.29%
VQGAN-LC (Zhu et al., 2024a)	16×16	16,384	8	3.01	<u>0.13</u>	<u>99%</u>
VQGAN-LC (Zhu et al., 2024a)	16×16	100,000	8	2.62	0.12	<u>99%</u>
IBQ† (Shi et al., 2025)	16×16	16,384	256	1.55	0.23	97%
FVQ	16×16	16,384	256	<u>1.30</u>	<u>0.13</u>	100%
FVQ‡	16×16	16,384	256	1.17	0.13	100%

Table 2: **Generative model comparison on class-conditional ImageNet 256×256 .** The metrics include Fréchet Inception Distance (FID), Inception Score (IS), Precision (Pre), and Recall (Rec). We highlight the best results in bold and underline the second-best results.

Type	Model	#Para	FID \downarrow	IS \uparrow	Pre \uparrow	Rec \uparrow
Diff.	DiT-L/2 (Peebles & Xie, 2023)	458M	5.02	167.2	0.75	0.57
Diff.	DiT-XL/2 (Peebles & Xie, 2023)	675M	<u>2.27</u>	278.2	0.83	0.57
Mask.	MaskGIT (Chang et al., 2022)	227M	6.18	182.1	0.80	0.51
VAR	VAR-d16 (Tian et al., 2024)	310M	3.30	274.4	0.84	0.51
VAR	VAR-d20 (Tian et al., 2024)	600M	2.57	302.6	<u>0.83</u>	0.56
AR	VQGAN (Esser et al., 2021)	227M	18.65	80.4	0.78	0.26
AR	LlamaGen-L (Sun et al., 2024)	343M	3.81	248.3	<u>0.83</u>	0.52
AR	LlamaGen-XL (Sun et al., 2024)	775M	3.39	227.1	0.81	0.54
AR	IBQ-B (Shi et al., 2025)	342M	2.88	254.4	0.84	0.51
AR	IBQ-L (Shi et al., 2025)	649M	2.45	267.5	0.83	0.52
AR	FVQ-L (LlamaGen-L)	343M	2.39	276.6	0.84	0.56
AR	FVQ-XL (LlamaGen-XL)	775M	2.07	287.0	<u>0.83</u>	0.58

Implementation Details. For visual reconstruction, we adopt a codebook with a size of 16,384 and a vector channel of 256. VQBridge is configured with a latent dimension of 256, a depth of 2 and a patch size of 16. The encoder and decoder configurations are identical to those in VQGAN (Esser et al., 2021; Sun et al., 2024), utilizing 2 layers of ResBlocks. The model is trained for 40 epochs with a base learning rate of 1e-4 and a batch size of 128. Learning annealing starts with a 4-epoch warmup, followed by a learning rate decay to 1% of the original value. The Adam optimizer (Kingma, 2014) is employed with $\beta_1 = 0.9$ and $\beta_2 = 0.95$. Finally, we scale the training time to 120 epochs. For visual generation, LlamaGen (Sun et al., 2024) is utilized as the generator, with training configurations aligned with the open-source implementations. Additional details are provided in the Appendix G.

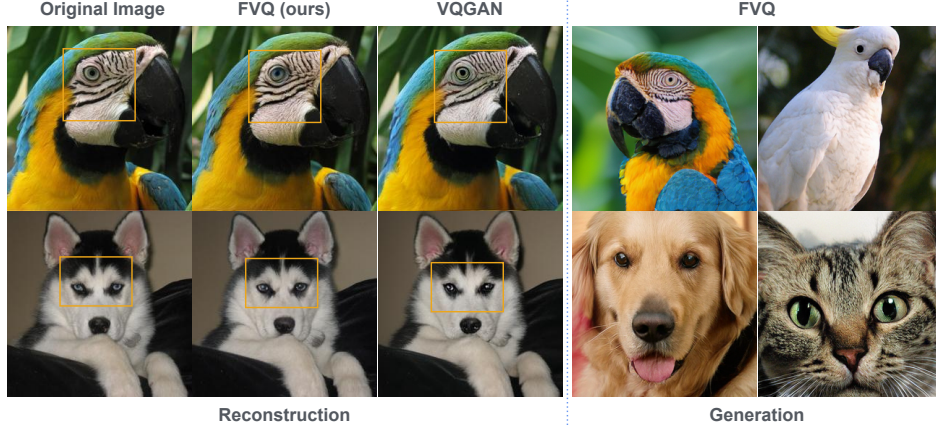


Figure 5: **Qualitative results of FVQ.** **Left:** reconstruction performance compared against baseline methods. **Right:** generation results.

Reconstruction Results. In Table 1, we compare existing tokenizers using the same encoder and decoder architectures, most of which are trained on ImageNet-1k 256x256 with a downsampling ratio of 16. FVQ achieves an rFID of 1.30 after 40 epochs, outperforming all other discrete tokenizers. Scaling the training time to 120 epochs further improves the rFID to 1.17. By addressing the optimization challenges of vector quantization, our method can be extended to other discrete tokenizers, unlocking their full potential (see Section 4.4).

Visual Generation. We report the results of LlamaGen (Sun et al., 2024) as generators in Table 2, comparing them with prior generative models. FVQ improves the FID of LlamaGen-L from 3.81 to 2.39, surpassing other models with similar parameter sizes. Notably, FVQ-L (343M) even outperforms VAR-d20 (600M, 2.39 vs. 2.57), and FVQ-XL exceeds DiT-XL/2 (2.07 vs. 2.27), demonstrating the potential of autoregressive (AR) methods. These results further emphasize that the tokenizer is the key to AR visual generation. Previous AR models are constrained by suboptimal tokenizers, whereas FVQ significantly enhances the generative capabilities of AR models, fully unlocking their potential. See Figure 5 for visualization results.

4.2 ABLATION STUDIES

To identify the most efficient and effective setup, we explore various settings of VQBridge in Figure 6, focusing on the interplay between its parameters, codebook’s size and vector channel.

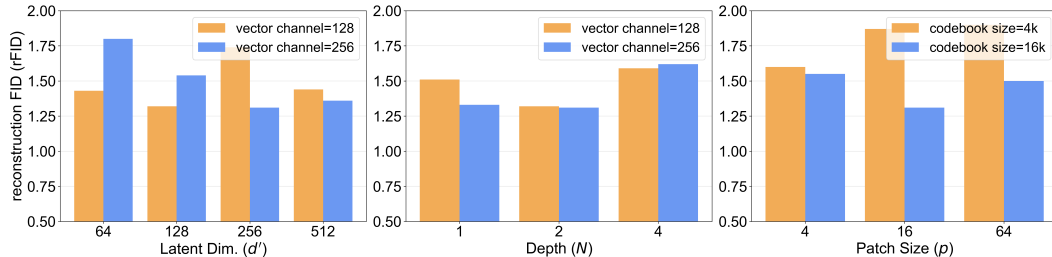


Figure 6: **VQBridge design ablation results.** We vary VQBridge configurations including the latent dimension (d'), ViT block depth (N), and patch size (p), as well as codebook parameters such as the vector channel and codebook size.

Latent Dimension (d'). In left subfigure, increasing d' from 64 to 256 consistently improves the reconstruction quality. Interestingly, the best results appear when the latent dimension d' matches the vector channel size, indicating that a balanced latent embedding dimension and code vector width facilitates more effective representation learning. Further enlarging d' to 512 does not provide additional benefits, and may even degrade performance due to over-parameterization and optimization difficulties. Therefore, we set d' equal to the vector channel size in our final configuration.

Depth of ViT Block (N). The middle subfigure shows that using a single ViT block leads to suboptimal results. Increasing the depth to $N = 2$ significantly improves performance, while further stacking blocks ($N = 4$) actually degrades performance due to increased optimization difficulty and higher computation cost. Therefore, $N = 2$ is adopted as our default.

Patch Size (p). The right subfigure presents the effect of patch size under different codebook sizes, with both parameters following a 4^n scaling pattern. Our experiments reveal a clear scaling relationship: when $K = 4k$, the optimal patch size is $p = 4$, while when $K = 16k$, the optimal patch size is $p = 16$, indicating that patch size and codebook size should be scaled together to achieve optimal performance. This scaling relationship reflects a balance between the computational pressure on the Patchify stage and the ViT blocks.

Our final model adopts latent dimension d' consistent with the vector channel dimension (default 256), 2 ViT blocks, and $p = 16$ with a $K = 16k$ codebook. When scaling up the codebook, we simultaneously increase the patch size by the same factor of $4\times$. This scaling strategy ensures optimal performance across different model configurations while preserving computational efficiency.

4.3 SCALING STUDIES

Table 3 presents a comprehensive evaluation of scalability across different model configurations, examining the effects of codebook size, vector channels, and training epochs on reconstruction quality and codebook usage. The results demonstrate performance differences between VQGAN and FVQ across multiple scaling dimensions. All models are trained on ImageNet (Deng et al., 2009) and evaluated on both the ImageNet val set (50k) and COCO 2017 val set (5k) (LAION, 2022).

Table 3: **Results of scalability from codebook size, vector channel and training epoch.** $rFID_{IN1K}$ denotes the results evaluated on the ImageNet-1k validation set, while $rFID_{COCO}$ denotes the results evaluated on the COCO validation set. (-Ann.) denotes results without learning annealing.

Model	Training Epoch	Ratio	Codebook Size	Vector Channel	$rFID_{IN1K}$	$rFID_{COCO}$	Usage
1 VQGAN	40	16	16k	8	2.19	8.43	97%
2 VQGAN	40	16	16k	256	9.21	—	0.29%
3 FVQ ^{-Ann.}	40	16	16k	256	2.61	—	100%
4 FVQ	40	16	16k	4	1.71	7.64	100%
5 FVQ	40	16	16k	8	1.47	7.15	100%
6 FVQ	40	16	16k	256	1.30	6.84	100%
7 FVQ	120	16	16k	256	1.17	6.62	100%
8 FVQ	40	16	65k	256	1.14	6.39	100%
9 FVQ	40	16	65k	512	1.09	6.38	100%
10 FVQ	120	16	65k	512	1.00	6.16	100%
11 FVQ	40	16	262k	256	0.95	6.04	100%
12 FVQ	120	16	262k	256	0.88	5.83	100%
13 VQGAN	40	8	16k	8	0.98	5.03	97%
14 FVQ	40	8	16k	256	0.39	3.84	100%

Model Performance and Stability. FVQ consistently outperforms VQGAN in both reconstruction quality and codebook usage. As shown in Figure 3, FVQ achieves 100% codebook usage early in training and maintains it throughout. Learning annealing further improves alignment in VQNs (from 2.61 to 1.30), as noted in **Observation 2**, which is also confirmed by our experiments. FVQ sustains full codebook usage across all tested configurations, whereas VQGAN experiences severe codebook collapse in high-capacity settings, with usage dropping to only 0.29% when employing 256 vector channels, validating **Observation 3**. This stability advantage is crucial for practical applications, as it ensures reliable performance scaling without catastrophic failure modes.

Codebook Size Scaling. Our experiments reveal clear scaling benefits with increased codebook capacity. For FVQ with 40 training epochs and 256 vector channels, expanding the codebook from 16k to 262k entries yields substantial improvements in reconstruction quality, with $rFID_{IN1K}$ decreasing from 1.30 to 0.95 and $rFID_{COCO}$ from 6.84 to 6.04. This trend indicates that larger codebooks provide enhanced representational capacity without suffering from underutilization issues.

Vector Channel Effects. Increasing vector channels from 4 to 256 leads to substantial improvements in reconstruction quality across both datasets. On ImageNet, $\text{rFID}_{\text{INIK}}$ decreases from 1.71 to 1.30, while on COCO, $\text{rFID}_{\text{COCO}}$ improves from 7.64 to 6.84. This trend demonstrates that higher-dimensional vector representations enable more expressive feature encoding, allowing the model to capture finer visual details and achieve better reconstruction fidelity. Importantly, these findings provide a crucial foundation for integrating a semantic tokenizer (*e.g.*, CLIP (Radford et al., 2021) with 512-dimensional embeddings) with vector quantization.

Training Duration Impact. Extending training from 40 to 120 epochs yields consistent but diminishing returns on ImageNet, while on COCO it results in steady improvements, with $\text{rFID}_{\text{COCO}}$ increasing by approximately 0.2 at each evaluation interval.

Compression Trade-offs. Higher compression ratios (*e.g.*, 16 \times) make the reconstruction task more challenging, reducing reconstruction quality, while lower compression ratios (*e.g.*, 8 \times) facilitate learning and improve reconstruction fidelity. Both models benefit from reduced compression, but FVQ maintains its stability advantage across compression levels, achieving $\text{rFID}_{\text{INIK}}$ of 0.39 and $\text{rFID}_{\text{COCO}}$ of 3.84 at 8 \times compression with full codebook usage.

These findings establish FVQ as a more scalable and reliable architecture for vector quantization tasks, demonstrating predictable performance improvements with increased computational resources while maintaining full codebook usage across diverse configurations.

4.4 GENERALIZATION STUDIES

Recently, several multi-code representation methods have been proposed to improve VQ, where multiple tokens are used to represent a single spatial location (*e.g.*, RQ-VAE (Lee et al., 2022) and VAR (Tian et al., 2024)). To demonstrate the generalization ability of our approach, we further conduct experiments on these two methods.

Table 4: **Multi-Code Representation VQ.** 680_{10step} denotes a code map constructed through 10 sequential quantization steps with step sizes 1, 2, 3, 4, 5, 6, 8, 10, 13, 16, where 680 is the sum of squares of the sequence.

Method	Training Epoch	Token Map	Codebook Size	Vector Channel	$\text{rFID} \downarrow$
RQ-VAE (Lee et al., 2022)	10	$8 \times 8 \times 4$	16,384	256	4.73
RQ-VAE (Lee et al., 2022)	50	$8 \times 8 \times 4$	16,384	256	3.20
FVQ (RQ-VAE)	10	$8 \times 8 \times 4$	16,384	256	2.98
VAR (Tian et al., 2024)	40	680_{10step}	4,096	32	1.00
FVQ (VAR)	40	680_{10step}	16,384	256	0.80

We follow the original training protocols as closely as possible. The results are reported in Table 4, where our method consistently improves performance. Notably, with only 10 epochs of training, our approach surpasses RQ-VAE trained for 50 epochs. This highlights the strong generalization ability and training efficiency of our method.

5 CONCLUSION

We have systematically analyzed the challenges inherent in discrete tokenizers and identified the root causes of unstable training and codebook collapse. Based on these insights, we proposed FVQ with the VQBridge projector, enabling robust, scalable, and high-quality VQ optimization. Our experiments show that high codebook usage and state-of-the-art reconstruction are achievable across diverse settings, and that strong tokenizers are essential for effective autoregressive image generation. Beyond improving current models, our work provides a foundation for extending VQ training to larger-scale and potentially unlabeled datasets. We believe these findings will inform future research on autoregressive visual generation and contribute to the development of more capable multimodal learning systems.

REFERENCES

Alpha-VLLM. Large-dit-imagenet. <https://github.com/Alpha-VLLM/LLaMA2-Accessory/tree/f7fe19834b23e38f333403b91bb0330afe19f79e/Large-DiT-ImageNet>, 2024.

Jinze Bai, Shuai Bai, Yunfei Chu, Zeyu Cui, Kai Dang, Xiaodong Deng, Yang Fan, Wenbin Ge, Yu Han, Fei Huang, et al. Qwen technical report. *arXiv preprint arXiv:2309.16609*, 2023.

Yoshua Bengio, Nicholas Léonard, and Aaron Courville. Estimating or propagating gradients through stochastic neurons for conditional computation. *arXiv preprint arXiv:1308.3432*, 2013.

Andrew Brock, Jeff Donahue, and Karen Simonyan. Large scale gan training for high fidelity natural image synthesis. *arXiv preprint arXiv:1809.11096*, 2018.

Tom Brown, Benjamin Mann, Nick Ryder, Melanie Subbiah, Jared D Kaplan, Prafulla Dhariwal, Arvind Neelakantan, Pranav Shyam, Girish Sastry, Amanda Askell, Sandhini Agarwal, Ariel Herbert-Voss, Gretchen Krueger, Tom Henighan, Rewon Child, Aditya Ramesh, Daniel Ziegler, Jeffrey Wu, Clemens Winter, Chris Hesse, Mark Chen, Eric Sigler, Mateusz Litwin, Scott Gray, Benjamin Chess, Jack Clark, Christopher Berner, Sam McCandlish, Alec Radford, Ilya Sutskever, and Dario Amodei. Language models are few-shot learners. In *NeurIPS*, volume 33, pp. 1877–1901, 2020.

Huiwen Chang, Han Zhang, Lu Jiang, Ce Liu, and William T. Freeman. Maskgit: Masked generative image transformer. In *CVPR*, pp. 11305–11315, 2022.

Mark Chen, Alec Radford, Rewon Child, Jeffrey Wu, Heewoo Jun, David Luan, and Ilya Sutskever. Generative pretraining from pixels. In *ICML*, pp. 1691–1703. PMLR, 2020.

Jia Deng, Wei Dong, Richard Socher, Li-Jia Li, Kai Li, and Li Fei-Fei. ImageNet: A large-scale hierarchical image database. In *CVPR*, pp. 248–255, 2009.

Jacob Devlin, Ming-Wei Chang, Kenton Lee, and Kristina Toutanova. Bert: Pre-training of deep bidirectional transformers for language understanding. *arXiv preprint arXiv:1810.04805*, 2018.

Prafulla Dhariwal and Alexander Nichol. Diffusion models beat gans on image synthesis. *NeurIPS*, 34: 8780–8794, 2021.

Alexey Dosovitskiy, Lucas Beyer, Alexander Kolesnikov, Dirk Weissenborn, Xiaohua Zhai, Thomas Unterthiner, Mostafa Dehghani, Matthias Minderer, G Heigold, S Gelly, et al. An image is worth 16x16 words: Transformers for image recognition at scale. In *ICLR*, 2020.

Patrick Esser, Robin Rombach, and Björn Ommer. Taming transformers for high-resolution image synthesis. In *CVPR*, pp. 12873–12883, 2021.

Aaron Grattafiori, Abhimanyu Dubey, Abhinav Jauhri, Abhinav Pandey, Abhishek Kadian, Ahmad Al-Dahle, Aiesha Letman, Akhil Mathur, Alan Schelten, Alex Vaughan, et al. The llama 3 herd of models. *arXiv preprint arXiv:2407.21783*, 2024.

Jonathan Ho, Ajay Jain, and Pieter Abbeel. Denoising diffusion probabilistic models. *NeurIPS*, 33:6840–6851, 2020.

Jonathan Ho, Chitwan Saharia, William Chan, David J Fleet, Mohammad Norouzi, and Tim Salimans. Cascaded diffusion models for high fidelity image generation. *JMLR*, 23(1):2249–2281, 2022.

Minyoung Huh, Brian Cheung, Pulkit Agrawal, and Phillip Isola. Straightening out the straight-through estimator: Overcoming optimization challenges in vector quantized networks. In *International Conference on Machine Learning*, pp. 14096–14113. PMLR, 2023.

Phillip Isola, Jun-Yan Zhu, Tinghui Zhou, and Alexei A. Efros. Image-to-image translation with conditional adversarial networks. In *CVPR*, pp. 5967–5976, 2017.

Minguk Kang, Jun-Yan Zhu, Richard Zhang, Jaesik Park, Eli Shechtman, Sylvain Paris, and Taesung Park. Scaling up gans for text-to-image synthesis. In *CVPR*, pp. 10124–10134, 2023.

Diederik P Kingma. Auto-encoding variational bayes. *arXiv preprint arXiv:1312.6114*, 2013.

Diederik P Kingma. Adam: A method for stochastic optimization. *arXiv preprint arXiv:1412.6980*, 2014.

Alina Kuznetsova, Hassan Rom, Neil Alldrin, Jasper Uijlings, Ivan Krasin, Jordi Pont-Tuset, Shahab Kamali, Stefan Popov, Matteo Malloci, Alexander Kolesnikov, et al. The open images dataset v4: Unified image classification, object detection, and visual relationship detection at scale. *IJCV*, 128(7):1956–1981, 2020.

LAION. Laion-coco 600m. <https://laion.ai/blog/laion-coco>, 2022.

Adrian Łaniczki, Jan Chorowski, Guillaume Sanchez, Ricard Marxer, Nanxin Chen, Hans JGA Dolfing, Sameer Khurana, Tanel Alumäe, and Antoine Laurent. Robust training of vector quantized bottleneck models. In *2020 International Joint Conference on Neural Networks (IJCNN)*, pp. 1–7. IEEE, 2020.

Doyup Lee, Chiheon Kim, Saehoon Kim, Minsu Cho, and Wook-Shin Han. Autoregressive image generation using residual quantization. In *CVPR*, pp. 11513–11522, 2022.

Tianhong Li, Dina Katabi, and Kaiming He. Return of unconditional generation: A self-supervised representation generation method. *NeurIPS*, 37:125441–125468, 2024a.

Tianhong Li, Yonglong Tian, He Li, Mingyang Deng, and Kaiming He. Autoregressive image generation without vector quantization. *arXiv preprint arXiv:2406.11838*, 2024b.

Yaron Lipman, Ricky TQ Chen, Heli Ben-Hamu, Maximilian Nickel, and Matt Le. Flow matching for generative modeling. *arXiv preprint arXiv:2210.02747*, 2022.

Zhuoyan Luo, Fengyuan Shi, Yixiao Ge, Yujiu Yang, Limin Wang, and Ying Shan. Open-magvit2: An open-source project toward democratizing auto-regressive visual generation. *arXiv preprint arXiv:2409.04410*, 2024.

Chuofan Ma, Yi Jiang, Junfeng Wu, Jihan Yang, Xin Yu, Zehuan Yuan, Bingyue Peng, and Xiaojuan Qi. Unitok: A unified tokenizer for visual generation and understanding. *arXiv preprint arXiv:2502.20321*, 2025.

Fabian Mentzer, David Minnen, Eirikur Agustsson, and Michael Tschannen. Finite scalar quantization: Vq-vae made simple. *arXiv preprint arXiv:2309.15505*, 2023.

Ziqi Pang, Tianyuan Zhang, Fujun Luan, Yunze Man, Hao Tan, Kai Zhang, William T Freeman, and Yu-Xiong Wang. Randar: Decoder-only autoregressive visual generation in random orders. *arXiv preprint arXiv:2412.01827*, 2024.

William Peebles and Saining Xie. Scalable diffusion models with transformers. In *CVPR*, pp. 4195–4205, 2023.

Alec Radford, Karthik Narasimhan, Tim Salimans, Ilya Sutskever, et al. Improving language understanding by generative pre-training. *article*, 2018.

Alec Radford, Jong Wook Kim, Chris Hallacy, Aditya Ramesh, Gabriel Goh, Sandhini Agarwal, Girish Sastry, Amanda Askell, Pamela Mishkin, Jack Clark, et al. Learning transferable visual models from natural language supervision. In *ICML*, pp. 8748–8763. PMLR, 2021.

Aditya Ramesh, Mikhail Pavlov, Gabriel Goh, Scott Gray, Chelsea Voss, Alec Radford, Mark Chen, and Ilya Sutskever. Zero-shot text-to-image generation. In Marina Meila and Tong Zhang (eds.), *ICML*, volume 139, pp. 8821–8831, 2021.

Ali Razavi, Aaron Van den Oord, and Oriol Vinyals. Generating diverse high-fidelity images with vq-vae-2. In *NeurIPS*, volume 32, 2019.

Robin Rombach, Andreas Blattmann, Dominik Lorenz, Patrick Esser, and Björn Ommer. High-resolution image synthesis with latent diffusion models. In *CVPR*, pp. 10684–10695, 2022a.

Robin Rombach, Andreas Blattmann, Dominik Lorenz, Patrick Esser, and Björn Ommer. High-resolution image synthesis with latent diffusion models. In *CVPR*, pp. 10674–10685, 2022b.

Axel Sauer, Katja Schwarz, and Andreas Geiger. Stylegan-xl: Scaling stylegan to large diverse datasets. In *SIGGRAPH*, pp. 1–10, 2022.

Fengyuan Shi, Zhuoyan Luo, Yixiao Ge, Yujiu Yang, Ying Shan, and Limin Wang. Taming scalable visual tokenizer for autoregressive image generation. *arXiv preprint arXiv:2412.02692*, 2025.

Jiaming Song, Chenlin Meng, and Stefano Ermon. Denoising diffusion implicit models. *arXiv preprint arXiv:2010.02502*, 2020.

Peize Sun, Yi Jiang, Shoufa Chen, Shilong Zhang, Bingyue Peng, Ping Luo, and Zehuan Yuan. Autoregressive model beats diffusion: Llama for scalable image generation. *arXiv preprint arXiv:2406.06525*, 2024.

Keyu Tian, Yi Jiang, Zehuan Yuan, Bingyue Peng, and Liwei Wang. Visual autoregressive modeling: Scalable image generation via next-scale prediction. *arXiv preprint arXiv:2404.02905*, 2024.

Hugo Touvron, Thibaut Lavril, Gautier Izacard, Xavier Martinet, Marie-Anne Lachaux, Timothée Lacroix, Baptiste Rozière, Naman Goyal, Eric Hambro, Faisal Azhar, et al. Llama: Open and efficient foundation language models. *arXiv preprint arXiv:2302.13971*, 2023.

Aaron Van den Oord, Nal Kalchbrenner, Lasse Espeholt, Oriol Vinyals, Alex Graves, et al. Conditional image generation with pixelcnn decoders. *NeurIPS*, 29, 2016.

Aaron Van Den Oord, Oriol Vinyals, et al. Neural discrete representation learning. In *NeurIPS*, volume 30, 2017.

Jiahui Yu, Xin Li, Jing Yu Koh, Han Zhang, Ruoming Pang, James Qin, Alexander Ku, Yuanzhong Xu, Jason Baldridge, and Yonghui Wu. Vector-quantized image modeling with improved VQGAN. In *ICLR*, 2022.

Lijun Yu, Jose Lezama, Nitesh Bharadwaj Gundavarapu, Luca Versari, Kihyuk Sohn, David Minnen, Yong Cheng, Agrim Gupta, Xiuye Gu, Alexander G Hauptmann, Boqing Gong, Ming-Hsuan Yang, Irfan Essa, David A Ross, and Lu Jiang. Language model beats diffusion - tokenizer is key to visual generation. In *ICLR*, 2024a.

Qihang Yu, Mark Weber, Xueqing Deng, Xiaohui Shen, Daniel Cremers, and Liang-Chieh Chen. An image is worth 32 tokens for reconstruction and generation. *arXiv preprint arXiv:2406.07550*, 2024b.

Jiahui Zhang, Fangneng Zhan, Christian Theobalt, and Shijian Lu. Regularized vector quantization for tokenized image synthesis. In *CVPR*, pp. 18467–18476, 2023.

Richard Zhang, Phillip Isola, Alexei A. Efros, Eli Shechtman, and Oliver Wang. The unreasonable effectiveness of deep features as a perceptual metric. In *CVPR*, pp. 586–595, 2018.

Chuanxia Zheng and Andrea Vedaldi. Online clustered codebook. In *ICCV*, pp. 22798–22807, 2023.

Chuanxia Zheng, Tung-Long Vuong, Jianfei Cai, and Dinh Phung. Movq: Modulating quantized vectors for high-fidelity image generation. *Advances in Neural Information Processing Systems*, 35:23412–23425, 2022.

Lei Zhu, Fangyun Wei, Yanye Lu, and Dong Chen. Scaling the codebook size of vqgan to 100,000 with a utilization rate of 99%. *arXiv preprint arXiv:2406.11837*, 2024a.

Yongxin Zhu, Bocheng Li, Yifei Xin, and Linli Xu. Addressing representation collapse in vector quantized models with one linear layer. *arXiv preprint arXiv:2411.02038*, 2024b.

A RELATED WORK

Image Quantization. To convert image features into discrete tokens, VQ-VAE (Van Den Oord et al., 2017) maps encoded features to the nearest vectors in a learned codebook. VQ-VAE2 (Razavi et al., 2019) improves quantization with a hierarchical encoding strategy, and VQGAN (Esser et al., 2021) enhances perceptual quality via adversarial and perceptual losses. However, scaling the codebook size and vector channel often leads to codebook collapse—low usage and poor reconstruction. To mitigate this, ViT-VQGAN (Yu et al., 2022) reduces the vector channel and adds l_2 normalization to improve codebook usage. FSQ (Mentzer et al., 2023) and LFQ (Yu et al., 2024a) adopt similar low-channel designs to maintain usage with larger codebook. Reg-VQ (Zhang et al., 2023) introduces prior regularization, while CVQ (Zheng & Vedaldi, 2023) resets underused codebook entries. Yet, these methods still struggle when both size and channel are scaled, limiting reconstruction quality. Recently, (Huh et al., 2023) specifically analyzes the impact of the Straight-Through Estimator (Bengio et al., 2013). IBQ (Shi et al., 2025) achieves high usage with large codebook and high channel via index backpropagation. VQGAN-LC (Zhu et al., 2024a) initializes codebook with pretrained features and employs a linear projector to jointly transform embedding. SimVQ (Zhu et al., 2024b) further highlights the importance of joint transformation and provides theoretical support for linear mappings. We argue that scaling both the codebook size and vector channel requires strong projector to fully optimize the codebook and ensure effective usage.

Image Generation. PixelCNN (Van den Oord et al., 2016) and iGPT (Chen et al., 2020) generates RGB pixels in a scanning order. VQGAN (Esser et al., 2021) improves (Van den Oord et al., 2016; Chen et al., 2020) by using an autoregressive approach in the latent space of VQVAE (Van Den Oord et al., 2017). VQVAE2 (Razavi et al., 2019) and RQ-Transformer (Lee et al., 2022) adopt the same approach but with additional scales. MaskGIT (Chang et al., 2022) employs masked prediction similar to BERT (Devlin et al., 2018). LlamaGen (Sun et al., 2024) demonstrates that autoregressive generation is possible even without visual bias, while VAR (Tian et al., 2024) explores visual autoregressive generation using multi-scale methods. RandAR (Pang et al., 2024) trains transformer in random orders to improve performance. Additionally, diffusion models (Ho et al., 2020; Song et al., 2020; Lipman et al., 2022; Rombach et al., 2022a;b; Peebles & Xie, 2023) generate images by denoising from noise. MAR (Li et al., 2024b) uses diffusion loss to eliminate the vector quantization process.

B LIMITATIONS AND FUTURE WORK

We primarily focus on the VQVAE/VQGAN-based learning paradigm to validate the effectiveness of our method. The solutions to codebook collapse and unstable training are general and can be further applied to models like UniTok (Ma et al., 2025) for additional improvements. Additionally, we only use LlamaGen as the generator; employing other strategies, such as random order learning and parallel decoding, can further enhance the generative capabilities of AR models.

Pretraining Tokenizer. We plan to train more advanced discrete tokenizers on larger-scale datasets, such as OpenImages (Kuznetsova et al., 2020) and LAION-COCO (LAION, 2022), to further enhance the reconstruction capabilities of discrete tokenizers and create better conditions for autoregressive generation.

Unified Tokenizer. Our results demonstrate that the vector channel can be scaled to larger dimensions. This facilitates alignment with visual representation tokenizers like CLIP (Radford et al., 2021) (dim=512), enabling a unified tokenizer to accomplish both generative and understanding tasks.

We will explore these aspects in the future.

C ADDITIONAL EXPERIMENTS IN OBSERVATION

In Figure 7, VQ loss tends to stabilize at a lower value as the codebook size increases. Early in training, the loss drops quickly because only a few code vectors are active. This allows the encoder to fit the codebook entries easily. Additional results are reported in Table 5, which demonstrate the necessity of using VQBridge together with annealing.

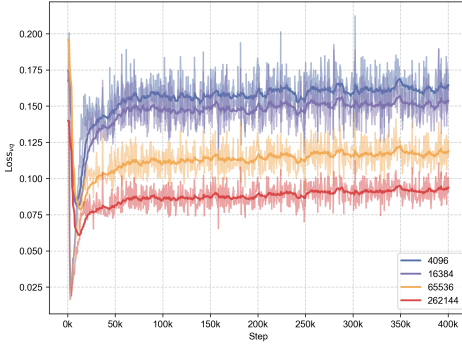


Figure 7: Effect of codebook size on training loss

Method	Codebook Size	usage	rFID
linear	16k	100%	2.10
linear+Annealing	16k	53%	1.52
VQBridge	16k	100%	2.61
VQBridge+Annealing	16k	100%	1.30
MLP-5	262k	20%	2.06
MLP-5+Annealing	262k	22%	1.75
VQBridge	262k	100%	1.40
VQBridge+Annealing	262k	100%	0.95

Table 5: Additional observational results.

D DERIVATION OF THE ONE-STEP-BEHIND FORMULA

Consider the t -th iteration of VQ training with the following components: encoder output $\mathbf{z}_e^{(t)} \in \mathbb{R}^d$, quantized output $\mathbf{z}_q^{(t)}$.

The Vector Quantization commitment loss is defined as:

$$\mathcal{L}_{\text{vq}} \left(\mathbf{z}_e^{(t)}, \mathbf{z}_q^{(t)} \right) = \frac{1}{2} \left\| \mathbf{z}_e^{(t)} - \mathbf{z}_q^{(t)} \right\|_2^2. \quad (12)$$

The gradient of the commitment loss with respect to the vector code \mathbf{z}_q is:

$$\frac{\partial \mathcal{L}_{\text{vq}} \left(\mathbf{z}_e^{(t)}, \mathbf{z}_q^{(t)} \right)}{\partial \mathbf{z}_q^{(t)}} = \frac{1}{2} \cdot 2 \left(\mathbf{z}_q^{(t)} - \mathbf{z}_e^{(t)} \right). \quad (13)$$

The update rule for $\mathbf{z}_q^{(t+1)}$ when optimizing with SGD is:

$$\mathbf{z}_q^{(t+1)} = \mathbf{z}_q^{(t)} - \eta \frac{\partial \mathcal{L}_{\text{vq}} \left(\mathbf{z}_e^{(t)}, \mathbf{z}_q^{(t)} \right)}{\partial \mathbf{z}_q^{(t)}}. \quad (14)$$

Substituting the gradient:

$$\mathbf{z}_q^{(t+1)} = \mathbf{z}_q^{(t)} - \eta \cdot \left(\mathbf{z}_q^{(t)} - \mathbf{z}_e^{(t)} \right). \quad (15)$$

Expanding and rearranging:

$$\mathbf{z}_q^{(t+1)} = \mathbf{z}_q^{(t)} - \eta \mathbf{z}_q^{(t)} + \eta \mathbf{z}_e^{(t)} = (1 - \eta) \cdot \mathbf{z}_q^{(t)} + \eta \cdot \mathbf{z}_e^{(t)}. \quad (16)$$

From the above, we arrive at Equation 6. The correct update is given by Equation 7, and we derive an executable formula following (Huh et al., 2023). First,

$$\mathbf{z}_e^{(t+1)} = \mathbf{z}_e^{(t)} - \eta \frac{\partial \mathcal{L}_{\text{task}}}{\partial \mathbf{z}_e} \Big|_t. \quad (17)$$

Substituting Equation 17 into Equation 7:

$$\mathbf{z}_q^{(t+1)} = (1 - \eta) \cdot \mathbf{z}_q^{(t)} + \eta \cdot \mathbf{z}_e^{(t+1)} \quad (18)$$

$$= (1 - \eta) \cdot \mathbf{z}_q^{(t)} + \eta \left(\mathbf{z}_e^{(t)} - \eta \frac{\partial \mathcal{L}_{\text{task}}}{\partial \mathbf{z}_e} \Big|_t \right) \quad (19)$$

$$= \underbrace{(1 - \eta) \cdot \mathbf{z}_q^{(t)} + \eta \cdot \mathbf{z}_e^{(t)}}_{\text{commitment loss}} - \eta^2 \frac{\partial \mathcal{L}_{\text{task}}}{\partial \mathbf{z}_e} \Big|_t. \quad (20)$$

It can be observed that the additional term is multiplied by η^2 . When annealing is applied, the contribution of this term is negligible, which underscores the importance of learning annealing.

E EFFECT OF ONE-STEP-BEHIND ON TRAINING STABILITY

In the $(t + 1)$ -th forward pass, quantization uses the *updated* codebook:

$$x^{(t+1)} = \arg \min_k \|\mathbf{z}_e^{(t+1)} - \mathbf{c}_k^{(t)}\|_2^2, \quad (21)$$

$$\mathbf{z}_q^{(t+1)} = \mathbf{c}_{x^{(t+1)}}^{(t)}. \quad (22)$$

Comparing with the quantization point used for backpropagation in step t : $\mathbf{z}_q^{(t)} = \mathbf{c}_{x^{(t)}}^{(t-1)}$, we observe a temporal misalignment: **Step t** encoder updates using signals around $\mathcal{C}^{(t-1)}$; **Step $t + 1$ forward** quantization centers have changed to $\mathcal{C}^{(t)}$. This inconsistency constitutes **one-step-behind problem**.

Mathematical Analysis. The quantization center shift can be expressed as:

$$\underbrace{\mathbf{z}_q^{(t+1)} - \mathbf{z}_q^{(t)}}_{\text{Quantization center shift}} = \mathbf{c}_{x^{(t+1)}}^{(t)} - \mathbf{c}_{x^{(t)}}^{(t-1)}. \quad (23)$$

This decomposes into two components:

$$= \underbrace{(\mathbf{c}_{x^{(t+1)}}^{(t)} - \mathbf{c}_{x^{(t+1)}}^{(t-1)})}_{\text{Codebook update effect}} + \underbrace{(\mathbf{c}_{x^{(t+1)}}^{(t-1)} - \mathbf{c}_{x^{(t)}}^{(t-1)})}_{\text{Cluster switching}}. \quad (24)$$

By the triangle inequality,

$$\|\mathbf{z}_q^{(t+1)} - \mathbf{z}_q^{(t)}\| \leq \|\mathbf{c}_{x^{(t+1)}}^{(t)} - \mathbf{c}_{x^{(t+1)}}^{(t-1)}\| + \|\mathbf{c}_{x^{(t+1)}}^{(t-1)} - \mathbf{c}_{x^{(t)}}^{(t-1)}\|. \quad (25)$$

Bounded Change Analysis. Assume bounded changes:

$$\|\mathbf{c}_i^{(t)} - \mathbf{c}_i^{(t-1)}\| \leq \delta_c \quad \forall i, \quad \|\mathbf{z}_e^{(t+1)} - \mathbf{z}_e^{(t)}\| \leq \delta_z. \quad (26)$$

Define the assignment margin at time t as the difference between the distances to the nearest and second-nearest centers (evaluated w.r.t. $\{\mathbf{c}_i^{(t-1)}\}$):

$$m^{(t)} := \|\mathbf{z}_e^{(t)} - \mathbf{c}_{2\text{nd}}^{(t-1)}\| - \|\mathbf{z}_e^{(t)} - \mathbf{c}_{1\text{st}}^{(t-1)}\|. \quad (27)$$

Using the triangle inequality one obtains that if $m^{(t)} > 2\delta_z$ then the nearest-center assignment is preserved (i.e. $x^{(t+1)} = x^{(t)}$); conversely, when $m^{(t)} \leq 2\delta_z$ cluster switching may occur. In the no-switching case

$$\|\mathbf{z}_q^{(t+1)} - \mathbf{z}_q^{(t)}\| \leq \delta_c, \quad (28)$$

while in the worst case (arbitrary switching) we may only guarantee

$$\|\mathbf{z}_q^{(t+1)} - \mathbf{z}_q^{(t)}\| \leq \delta_c + D_{\max}, \quad (29)$$

where $D_{\max} := \max_{i,j} \|\mathbf{c}_i^{(t-1)} - \mathbf{c}_j^{(t-1)}\|$ is a (time-local) upper bound on inter-center distances.

Finally, if the task loss \mathcal{L} is L -Lipschitz w.r.t. \mathbf{z}_q , then

$$|\mathcal{L}(\mathbf{z}_q^{(t+1)}) - \mathcal{L}(\mathbf{z}_q^{(t)})| \leq L \|\mathbf{z}_q^{(t+1)} - \mathbf{z}_q^{(t)}\|. \quad (30)$$

Combining the above yields the following interpretation: when encoder outputs lie away from cluster boundaries ($m^{(t)} > 2\delta_z$) and codebook updates are small (δ_c small), loss fluctuations induced by one-step-behind are controlled by $L\delta_c$; however, near boundaries cluster switching can produce center jumps of order inter-cluster distances, which the Lipschitz property amplifies into large loss fluctuations and thus destabilizes training.

Implication for the Decoder. Since the quantized vector \mathbf{z}_q is directly fed into the decoder, fluctuations in \mathbf{z}_q propagate to the reconstruction stage. In the stable case (no switching, small δ_c), the decoder receives smoothly varying inputs and can learn a consistent mapping. In contrast, when cluster switching occurs, \mathbf{z}_q may undergo discontinuous jumps of order D_{\max} , forcing the decoder to fit inconsistent latent representations across consecutive steps. This misalignment not only destabilizes optimization but also degrades reconstruction quality, as the decoder struggles to reconcile abrupt changes in its input space.

F VECTOR QUANTIZATION FOR IMAGE RECONSTRUCTION

A discrete tokenizer contains Encoder, Codebook and Decoder. Given an image $\mathbf{I} \in \mathbb{R}^{H \times W \times 3}$, the Encoder compresses it into an image feature map $\mathbf{Z} \in \mathbb{R}^{h \times w \times D}$, where $H \times W$ and $h \times w$ denote the spatial resolution of the image and feature map, D denotes the channel number of feature map. Formally,

$$\mathbf{Z} = \text{Encoder}(\mathbf{I}). \quad (31)$$

The Codebook contains K vectors $\mathcal{C} = \{\mathbf{c}_1, \mathbf{c}_2, \dots, \mathbf{c}_K\}$, where each vector \mathbf{c}_i is a D -dimensional vector. By searching for the most similar vector in the codebook, \mathbf{Z}_e is mapped to a feature \mathbf{Z}_q , and the indices form the token map \mathbf{T} . We denote the search process as $\text{Quant}(\cdot, \cdot)$. We have

$$\mathbf{c}_x = \text{Quant}(\mathbf{c}^{i,j}, \mathcal{C}), \quad (32)$$

where $x = \arg \min_{k \in \{1, 2, \dots, K\}} \|\mathbf{z}_e^{i,j} - \mathbf{c}_k\|_2$, and

$$\mathbf{Z}_q = \{\mathbf{c}_t^{i,j}\}, \mathbf{X} = \{x^{i,j}\}, \quad (33)$$

where $i \in \{1, \dots, h\}, j \in \{1, \dots, w\}$. The Decoder reconstructs \mathbf{Z}_q into $\hat{\mathbf{I}}$. Formally,

$$\hat{\mathbf{I}} = \text{Decoder}(\hat{\mathbf{Z}}), \quad (34)$$

Typically, a compound loss \mathcal{L} is optimized to train the model. We have

$$\mathcal{L} = \mathcal{L}_{rec} + \mathcal{L}_{commit} + \lambda_{perc} \mathcal{L}_{perc} + \lambda_G \mathcal{L}_G, \quad (35)$$

where $\mathcal{L}_{rec} = \|\mathbf{I} - \hat{\mathbf{I}}\|_2$, $\mathcal{L}_{commit} = \|sg[\mathbf{Z}_e] - \mathbf{Z}_q\|_2 + \beta \|sg[\mathbf{Z}_q] - \mathbf{Z}_e\|_2$, \mathcal{L}_{perc} is a perceptual loss like LPIPS (Zhang et al., 2018), \mathcal{L}_G is a discriminative loss like PatchGAN (Isola et al., 2017), β , λ_{perc} , λ_G are loss weights, and $sg[\cdot]$ is stop-gradient operation.

G FURTHER DETAILS ON EXPERIMENTAL CONFIGURATIONS

Table 6: **Experimental Configurations** on reconstruction and generation. Warmup(0.1) indicates that 10% of the training time is used for learning rate warmup.

Config	Reconstruction	Generation
Base Batch Size	128	256
Training Epochs	40 or 120	300–350
Optimizer	Adam	AdamW
Base Learning Rate	1×10^{-4}	1×10^{-4}
Learning Rate Schedule	warmup(0.1) [baselr(0.3)–linear(0.7)]	warmup(0) [baselr(0.05)–linear(0.95)]
Warmup Learning Rate	0.005 to 1	–
Linear Learning Rate	1 to 0.01	1 to 0.01
Optimizer Parameters	$\beta_1 = 0.9, \beta_2 = 0.95$	$\beta_1 = 0.9, \beta_2 = 0.95$ $weight_decay = 5 \times 10^{-2}$
Loss Weight	commit loss $\beta = 0.25$ perceptual loss $\lambda_{perc} = 1.0$ discriminative loss $\lambda_G = 0.5$	

The training recipe Table 6 follows LlamaGen (Sun et al., 2024), where the learning rate is calculated as (batch size / base batch size) \times base learning rate. The learning rate schedule specifies the proportions of different phases: warmup (0.1) indicates 10% of the training epochs, and [baselr(0.3)–linear(0.7)] represents the remaining 90%, with 30% maintaining a constant learning rate and 70% applying linear decay. All training is conducted on A100 GPUs, and evaluation follows the LlamaGen protocol. We use Fréchet Inception Distance (FID) as the primary metric, sampling 50,000 images and evaluating FID using code from ADM (Dhariwal & Nichol, 2021). Additionally, we report Inception Score (IS), Precision, and Recall.

H FURTHER RESULTS COMPARISON

Additional reconstruction results. We present results for more metrics, including RSNR and SSIM, in Table 7. We report additional comparison results in Table 8, highlighting the superiority of FVQ. As shown in the Table 8, FVQ achieves the best reconstruction performance (rFID=0.88) among all discrete tokenizers, outperforming Open-MAGVIT2 and IBQ, even though they utilize larger architectures.

Table 7: **Additional Metrics and Comparisons.** \ddagger trained for 120 epochs.

Method	Codebook Size	rFID \downarrow	RSNR \uparrow	SSIM \uparrow	Usage
LlamaGen (Sun et al., 2024)	16,384	2.19	20.79	0.675	97.0%
FVQ	16,384	1.30	22.36	0.648	100%
FVQ \ddagger	16,384	1.17	22.45	0.653	100%
FVQ	262,144	0.95	22.90	0.665	100%
FVQ \ddagger	262,144	0.88	22.95	0.672	100%

Table 8: **Reconstruction performance of different tokenizers on 256×256 ImageNet 50k validation set.** $*$ trained on OpenImages (Kuznetsova et al., 2020). \dagger trained for 330 epochs. \ddagger trained for 120 epochs. \diamond trained with 4 ResBlocks.

Method	Tokens	Codebook Size	Vector Channel	rFID \downarrow	LPIPS \downarrow	Codebook Usage \uparrow
VAE-SD* (Rombach et al., 2022a)	16×16		16	0.87	—	—
VAE-MAR (Li et al., 2024b)	16×16	—	16	1.22	—	—
<i>VQ-VAE-based Methods</i>						
VQGAN (Esser et al., 2021)	16×16	1,024	256	7.94	—	44%
VQGAN (Esser et al., 2021)	16×16	16,384	256	4.98	0.17	5.9%
VQGAN-SD* (Rombach et al., 2022a)	16×16	16,384	8	5.15	—	—
MaskGIT (Chang et al., 2022)	16×16	1,024	256	2.28	—	—
LlamaGen (Sun et al., 2024)	16×16	16,384	8	2.19	0.14	97%
LlamaGen (Sun et al., 2024)	16×16	16,384	256	9.21	—	0.29%
VQGAN-LC (Zhu et al., 2024a)	16×16	16,384	8	3.01	0.13	99%
VQGAN-LC (Zhu et al., 2024a)	16×16	100,000	8	2.62	0.12	99%
Open-MAGVIT2 $^{\dagger\diamond}$ (Luo et al., 2024)	16×16	16,384	0	1.58	0.23	100%
Open-MAGVIT2 $^{\dagger\diamond}$ (Luo et al., 2024)	16×16	262,144	0	1.17	0.20	100%
IBQ \dagger (Shi et al., 2025)	16×16	16,384	256	1.55	0.23	97%
IBQ $^{\dagger\diamond}$ (Shi et al., 2025)	16×16	16,384	256	1.37	0.22	96%
IBQ $^{\dagger\diamond}$ (Shi et al., 2025)	16×16	262,144	256	1.00	0.20	84%
FVQ	16×16	16,384	256	1.30	0.13	100%
FVQ \ddagger	16×16	16,384	256	1.17	0.13	100%
FVQ	16×16	262,144	256	0.95	0.12	100%
FVQ \ddagger	16×16	262,144	256	0.88	0.12	100%
<i>1-D Token Sequence</i>						
Titok-L (Yu et al., 2024b)	32	4,096	16	2.21	—	—
Titok-B (Yu et al., 2024b)	64	4,096	16	1.70	—	—
Titok-S (Yu et al., 2024b)	128	4,096	16	1.71	—	—
<i>Multi-Code Representation</i>						
RQ-VAE _{10ep} (Lee et al., 2022)	$8 \times 8 \times 4$	16,384	256	4.73	—	—
RQ-VAE _{50ep} (Lee et al., 2022)	$8 \times 8 \times 4$	16,384	256	3.20	—	—
MoVQ (Zheng et al., 2022)	$16 \times 16 \times 4$	1,024	64	1.12	—	—
VAR (Tian et al., 2024)	680_{10step}	4,096	32	1.00	—	—
FVQ (RQ-VAE _{10ep})	$8 \times 8 \times 4$	16,384	256	2.98	—	—
FVQ (VAR)	680_{10step}	16,384	256	0.80	—	—

Additional ablation experiments. We perform additional ablation experiments to study the effects of warmup and learning annealing. Our results indicate that warmup considerably influences performance, in line with the observations reported in (Huh et al., 2023). In contrast, the choice of learning annealing schedule—linear or cosine—has a negligible impact on the outcome. The detailed results are summarized in Table 9. Table 10 reports the computational cost of different projectors, highlighting the efficiency of VQBridge.

Table 9: Additional Ablation Experiments.

Method	Codebook Size	rFID
baseline w/ linear	16,384	1.30
w/o warmup	16,384	1.70
w/ cosine	16,384	1.32

Table 10: Estimated Model Computational Cost (in FLOPs)

Codebook Size	Linear	MLP-5	VQBridge
16,384	1.07G	5.37G	4.30G
262,144	17.18G	85.90G	55.89G

Additional generative results. We report more additional generative results in Table 11. FVQ-XL (775M, 2.07) surpasses VAR-d24 (1.0B, 2.09), RandAR-XXL (1.4B, 2.15) and L-DiT (3.0B, 2.10; 7.0B, 2.28), further demonstrating the importance of tokenizers and the superiority of AR methods. FVQ can also further enhance the capabilities of other AR models. Due to time and computational constraints, we plan to extend this work in the future.

Table 11: Generative model comparison on class-conditional ImageNet 256 × 256. The metrics include Fréchet Inception Distance (FID), Inception Score (IS), Precision (Pre), and Recall (Rec). [‡] trained with a learning rate schedule.

Type	Model	#Para	FID↓	IS↑	Pre↑	Rec↑
GAN	BigGAN (Brock et al., 2018)	112M	6.95	224.5	0.89	0.38
GAN	GigaGGAN (Kang et al., 2023)	569M	3.45	225.5	0.84	0.61
GAN	StyleGan-XL (Sauer et al., 2022)	166M	2.30	265.1	0.78	0.53
Diff.	ADM (Dhariwal & Nichol, 2021)	554M	10.94	101.0	0.69	0.63
Diff.	CDM (Ho et al., 2022)	—	4.88	158.7	—	—
Diff.	LDM-4-G (Rombach et al., 2022a)	400M	3.60	247.7	—	—
Diff.	DiT-L/2 (Peebles & Xie, 2023)	458M	5.02	167.2	0.75	0.57
Diff.	DiT-XL/2 (Peebles & Xie, 2023)	675M	2.27	278.2	0.83	0.57
Diff.	L-DiT-3B (Alpha-VLLM, 2024)	3.0B	2.10	304.4	0.82	0.60
Diff.	L-DiT-7B (Alpha-VLLM, 2024)	7.0B	2.28	316.2	0.83	0.58
Mask.	MaskGIT (Chang et al., 2022)	227M	6.18	182.1	0.80	0.51
Mask.	RCG (Li et al., 2024a)	502M	3.49	215.5	—	—
MAR	MAR-L (Li et al., 2024b)	479M	1.98	290.3	—	—
MAR	MAR-H (Li et al., 2024b)	943M	1.55	303.7	0.81	0.62
VAR	VAR-d16 (Tian et al., 2024)	310M	3.30	274.4	0.84	0.51
VAR	VAR-d20 (Tian et al., 2024)	600M	2.57	302.6	0.83	0.56
VAR	VAR-d24 (Tian et al., 2024)	1.0B	2.09	321.9	0.82	0.59
VAR	VAR-d30 (Tian et al., 2024)	2.0B	1.92	323.1	0.82	0.59
AR	VQGAN (Esser et al., 2021)	227M	18.65	80.4	0.78	0.26
AR	ViTVQ (Yu et al., 2022)	1.7B	4.17	175.1	—	—
AR	RQTran. (Lee et al., 2022)	3.8B	7.55	134.0	—	—
AR	RandAR-L (Pang et al., 2024)	343M	2.55	288.9	0.81	0.58
AR	RandAR-XL (Pang et al., 2024)	775M	2.25	317.8	0.80	0.60
AR	RandAR-XXL (Pang et al., 2024)	1.4B	2.15	321.9	0.79	0.60
AR	LlamaGen-L (Sun et al., 2024)	343M	3.81	248.3	0.83	0.52
AR	LlamaGen-XL (Sun et al., 2024)	775M	3.39	227.1	0.81	0.54
AR	LlamaGen-XXL (Sun et al., 2024)	1.4B	3.09	253.6	0.83	0.53
AR	IBQ-B (Shi et al., 2025)	342M	2.88	254.4	0.84	0.51
AR	IBQ-L (Shi et al., 2025)	649M	2.45	267.5	0.83	0.52
AR	IBQ-XL (Shi et al., 2025)	1.1B	2.14	279.0	0.83	0.56
AR	FVQ-L (LlamaGen-L)	343M	2.39	275.8	0.84	0.56
AR	FVQ-XL (LlamaGen-XL)	775M	2.07	287.0	0.83	0.58

I FURTHER VISUALIZATION ANALYSIS

Qualitative Reconstruction and Generation Samples. We present reconstruction samples in Figure 8 and generation samples in Figure 9-Figure 11.



Figure 8: FVQ-16,384 (rFID=1.17) reconstruction samples.



Figure 9: 256×256 FVQ-XL (FID=2.07) samples. Classifier-free guidance scale=1.65.

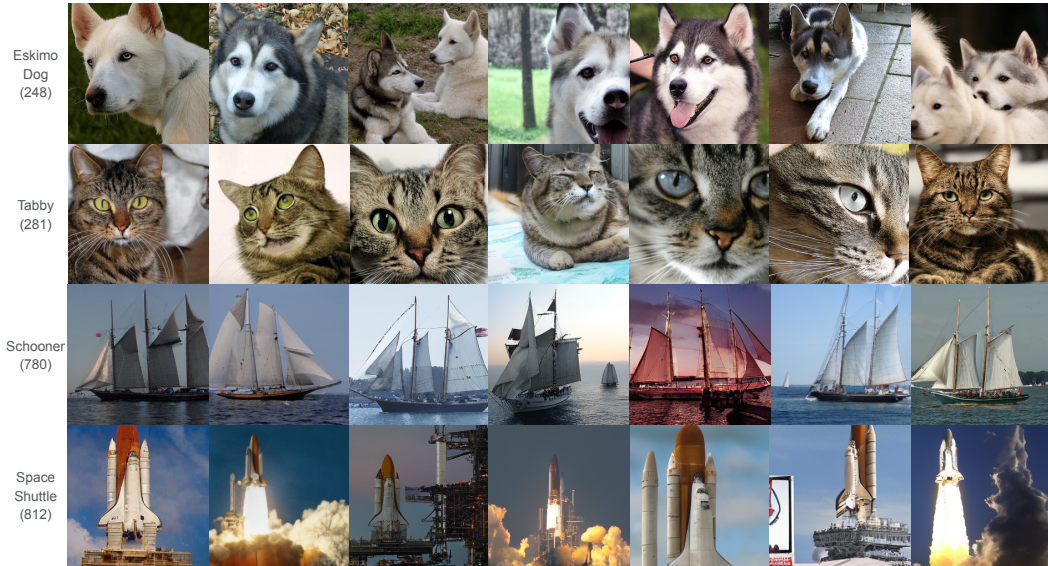


Figure 10: 256×256 **FVQ-XL (FID=2.07)** samples. Classifier-free guidance scale=1.65.



Figure 11: 256×256 **FVQ-XL (FID=2.07)** samples. Classifier-free guidance scale=1.65.